UNIVERSITY OF ST ANDREWS

MASTERS THESIS

Exploring the origins of bimodality: post-starburst galaxies at $z < 0.1$

Author:
John R. WEAVER

Supervisor:
Dr. Vivienne WILD

130011109

A thesis submitted in fulfillment of the requirements for the degree of Master of Physics (Honours) Astrophysics

in the

Astronomy Group
School of Physics & Astronomy

May 4th, 2018

"You heavenly powers, since you were responsible for those changes, as for all else, look favourably on my attempts, and spin an unbroken thread of verse, from the earliest beginnings of the world, down to my own times"

Ovid (1955, 29)

UNIVERSITY OF ST ANDREWS

Abstract

Faculty of Science & Medicine

School of Physics & Astronomy

Master of Physics (Honours) Astrophysics

Exploring the origins of bimodality:
post-starburst galaxies at $z < 0.1$

by John R. WEAVER

Post-starburst Galaxies (PSBs) are characterised by a lack of massive, young blue stars and a large fraction of intermediate mass A- and F-type stars. They are interpreted as a population of galaxies which have recently undergone a major episode of star formation, and their study may elucidate the nature of galaxy bimodality.

We employ a principal component analysis to study a sample of 32 low redshift (0.01 < z < 0.11) PSBs selected with SDSS DR 7 single-fibre spectroscopy and observed with MaNGA integral field spectroscopy. Morphologies are examined to characterise the sample, finding a mixture of starforming and quiescent parameters, indicative of transition. We find that this rich sample exhibits strong radial gradients in stellar age, as measured by the principal components (PC) corresponding to the 4000-Å break strength and excess Hδ absorption. To examine the extent of aperture bias, we compare these two properties between the DR 7 and MaNGA spectra, integrated over 3" and the full aperture, finding evidence for systematics and radial gradients. We employ two stellar population synthesis codes (BC03, FSPS) to test the manner in which star-formation proceeded, either as a single radially evolving burst, or coeval with varying burst strengths.

Achieved here for the first time, we find a remarkable consistency between the models and gradients, suggesting complex and diverse star-formation histories. We show that this method, coupled with an increased sample size, is well-suited to elucidate the real nature of these strange and peculiar objects.

Acknowledgements

Firstly, I would like to express my sincere gratitude to my supervisor, Dr. Vivienne Wild, for her constant encouragement, motivation, and direction. Both her guidance and insight have been invaluable throughout the research process and the writing of this thesis.

Besides my advisor, I would like to thank my main collaborators: Dr. Milena Pawlik and Dr. Kate Rowlands. It is only through their contributions to the ancillary data products that this work has been made possible. Many thanks for your patience when dealing with my many requests.

And to the members of the SDSS meeting group for their support, advice, and willingness to discuss to my research: Dr. Rita Tojeiro, Dr. Anne-Marie Weijmans, as well as Dominic Bates and Chris Duckworth. Thank you for sharing your perspectives and fielding my many questions.

Not to forget previous mentors and supervisors: Dr. Bernd Husemann, Dr. Michael Maseda, Dr. Michael West, Dr. Michael Gregg, Dr. Leslie Brown, Scott MacNeill, and Bruce Levine. Thank you for cultivating my interest in extragalactic astrophysics over the years. And a much deserved thank you to Prof. Keith Horne, for inspiring my enjoyment of astronomical statistics, which will forever shape my perspective on proper data analysis.

Thank you to my close friends for the many late nights spent over protracted discussions and my incoherent babbling, about astronomy, science, and life at large: Alisa Danilenko, Alastair Marshall, Didrik Willadssen, and Hayden Goodfellow. Your encouragement has not gone unnoticed or unappreciated.

I also wish to thank the pioneering astronomers who recognised the "island galaxies" and brought this field into existence less than a century ago: Dr. Edwin Hubble, Milton Humeson, Vesto Slipher, and Henrietta Leavitt.

And lastly, to my parents, for their unwavering support for my interest in the sciences, including long drives to extracurricular classes, early-morning pick ups from the observatory, and the increased shelf space around the house. Who could have imagined that a brief glance through a telescope could have led to all of this? For all, my love and sincere appreciation.

This research made use of the PYTHON packages `numpy` (Oliphant, 2015), `matplotlib` (Hunter, 2007), and `astropy` (Astropy Collaboration et al., 2013) Funding for the Sloan Digital Sky Survey IV has been provided by the Alfred P. Sloan Foundation, the U.S. Department of Energy Office of Science, and the Participating Institutions. SDSS-IV acknowledges support and resources from the Center for High Performance Computing at the University of Utah. The SDSS web site is www.sdss.org.

Contents

1 Introduction

The observed bimodality of galaxies is a key component of our Universe. It is expressed in extensively correlated morphologies, optical colours, and star-formation rate (SFR). While star-forming galaxies exhibit disc-like spiral structure, blue colours, and enhanced SFR; quiescents exhibit oblate elliptical structure, red colours, and little star formation (e.g. Strateva et al., 2001; Kauffmann et al., 2003; Bell et al., 2004; Baldry et al., 2004, 2006; Bundy et al., 2005). Although long-studied, the origins of galaxy bimodality remain elusive.

Investigations into the correlation between colour and absolute magnitude of galaxies have been fruitful (Bell et al., 2004; Baldry et al., 2004). Modern interpretations of this colour-magnitude diagram of galaxies have replaced colour with SFR (i.e. colour-age relation of stars) and absolute magnitude with stellar mass (M_*) (i.e. mass-to-light ratio). As shown in Fig. 1.1, Blue star-forming galaxies appear clumped in a region of enhanced SFR and low masses known as the *blue cloud*, and red passive galaxies appear strung along a locus of low SFR and high mass called the *red sequence*. The locus of this plane is known as the Star-formation Main Sequence (SFMS; Brinchmann et al., 2004; Daddi et al., 2007; Noeske et al., 2007; Salim et al., 2007; Rodighiero et al., 2011; Whitaker et al., 2012, 2014; Speagle et al., 2014; Rodighiero et al., 2014; Schreiber et al., 2015) .

Observation has concluded that while the mass density of the blue cloud has remained constant since $z\sim1$, the mass and number density of the red sequence has since doubled (e.g. Bell et al., 2004; Arnouts et al., 2007; Faber et al., 2007). Thus, the interpretation of bimodality is made clear: the mass assembly of massive quiescent galaxies is due to merger events, which shut off star formation (e.g. Daddi et al., 2010; Bouché et al., 2010; Genzel et al., 2010; Tacconi et al., 2010; Davé et al., 2012; Lilly et al., 2013; Dekel et al., 2013; Dayal et al., 2013; Feldmann, 2015; Tacchella et al., 2016).

The transition between the blue cloud and red sequence is marked by star-formation cessation or 'quenching'. Galaxies observed during this short-lived phase seem to exhibit features of both star-forming and quiescent galaxies, and fall between the blue cloud and red sequence in a region called the 'green valley' (Salim et al., 2007; Smethurst et al., 2015; Coenda et al., 2018). The diversity of morphologies found within the green valley have complicated attempts to probe the physical processes involved (Schawinski et al., 2014), and recent findings suggest that several pathways may exist.

Two types of processes have been identified to explain star-formation cessation: *internal* and *external* quenching. Firstly, internal quenching is due to secular processes within a galaxy, such as central compaction (Fang et al., 2013; Liu et al., 2016; Barro et al., 2017; Whitaker et al., 2017), feedback by an active galactic nucleus (AGN) (Croton et al., 2006), and supernovae wind (Geach et al., 2014); these effects scale with M_* ("mass-quenching"; e.g. Peng et al., 2010). They are centrally concentrated effects, causing cessation to proceed from the centre outwards via *inside-out* quenching. The

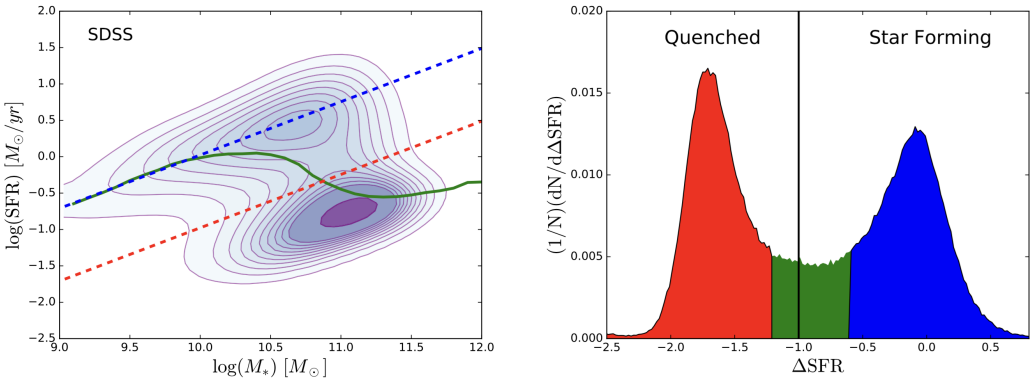

FIGURE 1.1: The Star-Forming Main Sequence (SFMS). **Left:** Logarithmic contour density diagram of a sample of SDSS galaxies, with the locus of the blue cloud and the red sequence shown dotted. The green solid line indicates the median relationship along the SFMS. **Right:** Histogram distribution for the difference in star formation from the SFMS (ΔSFR) for each galaxy. Figure adopted from Bluck et al. (2016).

second, external quenching, is due to environmental interaction (e.g. Peng et al., 2012; Geha et al., 2012; Guo et al., 2017), in turn stripping the gas reservoir from the *outside-in*. Liu et al. (2018) finds that at $z \sim 0.5 - 1$ these two channels are mass-segregated as galaxies with $M_* \leq 10^{10}\, M_\odot$ quench outside-in, and for $M_* > 10^{10.5}\, M_\odot$, they quench inside-out. The dominance and mass-bias of these two processes likely changes over cosmic time.

These two processes can be more readily distinguished by examining mass assembly as traced by gradients in sSFR (SFR/M_*), which provide information about star-formation strength, and trace the the pattern and propagation direction of the preceding starbust episode. The key then is to identify samples of galaxies who have recently ceased star-formation following a major burst, known as post-starbursts.

Post-starbust galaxies can be identified by characteristically weak nebular emission lines (i.e. little star formation), strong Balmer absorption lines typical of post-OB type stellar populations, and a strong 4000-Å break region. Together, these properties strongly suggest that these objects are recovering from a recent ($<$ 1Gyr) burst of star-formation. Many can be classified into the green valley based on optical colours. Hence, they represent an ideal sample with which to explore the several proposed mechanisms of star-formation cessation, and the direction of its propagation.

We leverage the power of Principal Component Analysis and spatially-resolved spectroscopic survey MaNGA to map and model the sSFR radial gradients observed in a large sample of 32 single-fibre-selected post-starbust galaxies. We characterise the sample using common morphological parameters to measure the light and matter distribution, with comparisons to standard populations of star-forming and quiescent galaxies. We also examine the effect of aperture bias within our sample, being able to compare the spectra from single-fibre selection to the MaNGA aperture. Lastly, we apply stellar synthesis models, varying the assumed underlying populations and burst mass fractions, gaining significant insight into the nature of the quenching event.

Throughout the paper we adopt a typical concordance cosmological model with $H_0 = 70\,\mathrm{km\,s^{-1}Mpc^{-1}}$, $\Omega_\mathrm{m} = 0.3$, and $\Omega_\Lambda = 0.7$.

2 Methods

2.1 Sample Selection

The extremely short timescales over which post-starbust galaxies (PSB) are thought to exist ($\sim$ 1Gyr) implies that these objects are extremely rare. Thus, the key lies in leveraging massively multiplexed surveys, such as the prolific Sloan Digital Sky Survey (SDSS), to provide the largest possible sample of PSBs to study. Within the nearby universe ($z < 0.1$), single-fibre spectroscopic studies of these galaxies have provided the basis for our understanding of the astrophysics, as revealed by morphology, metallicity, ionisation, and star formation. However, studies relying solely on single fibre spectroscopy are limited; a single spectrum can only provide information on the integrated light of the centres of galaxies.

The invention of spatially-resolved integral field spectroscopy has provided a way forward, revealing a galaxy not only as a function of wavelength, but also as a function of position. With a significantly increased field-of-view, such studies enable the mapping of stellar populations, velocity of stars and gas, ionisation states, metalicity, and star formation. Integral field units can vary in their spectral coverage, field-of-view (FoV), and spatial and spectral resolution. Past and current facilities such as VIMOS (Le Fèvre et al., 2003) and MUSE (Bacon et al., 2010) on the Very Large Telescope combine wide FoVs and integral field to provide exquisitely resolved studies of nearby galaxies, or for low-resolution multi-object studies of hundreds of galaxies in a single exposure.

With increased sample sizes and while retaining spatial resolution, multi-object fibre-optic integral-field surveys have provided massively multiplexed, deep studies of several thousand galaxies. Only recently has this technology become available, leading first with SAMI (Croom et al., 2012) observing 3400 galaxies, and continuing with MaNGA (Bundy et al., 2015). The power of these surveys lies in their use of Integral Field Units (IFU); pluggable fibre bundles of various sizes (Drory et al., 2015). To date, MaNGA has provided resolved maps of the stellar and gaseous components for more than 40,000 galaxies, with an additional 60,000 to be observed by its scheduled completion in 2020. MaNGA has already played a critical role in establishing key morphological and evolutionary trends of galaxies out to intermediate redshifts, only possible with spatially resolved spectroscopy (e.g. Li et al., 2015; Jin et al., 2016; Belfiore et al., 2016).

We select a sample of galaxies observed by the 6^{th} MaNGA Product Launch (MPL-6), with the condition that they were previously classified as post-starburst from the single-fibre spectroscopy survey of the SDSS Data Release 7 (DR 7). The reason for this is two-fold. Firstly, the pre-existing classifications from DR 7 allow for a more complete understanding of the sample's morphology, dust content, and AGN-status without additional study. Secondly, it allows for a one-to-one comparison between the

aperture-limited DR 7 spectra of the central bulges and the wider aperture MaNGA integral field spectra, an investigation of which may reveal important information about aperture bias and the nature of central and global post-starburst galaxies.

The selection procedure is comprised of a simple two-point correlation analysis with ASTROPY. The 33 objects found coincident within 1" were accepted as matches. One object ('8718-6101') was removed due to apparent contamination within the MaNGA FoV, leaving a final total of 32 objects. As shown in Fig. 2.1, the sample spans the MaNGA on-sky footprint. Also, the sample spans in redshift $0.1 < z < 0.11$, as shown in Fig. 2.2. This span is representative of the objects included in DR 7.

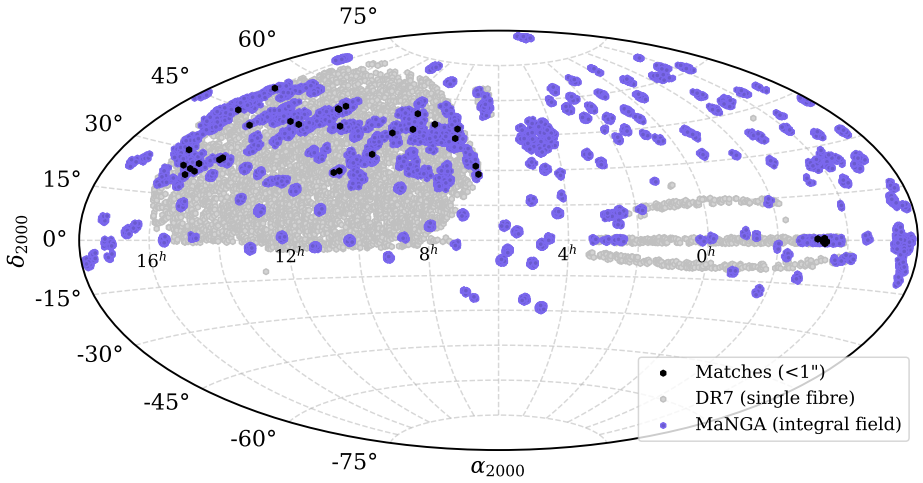

FIGURE 2.1: Survey and sample selection summary.

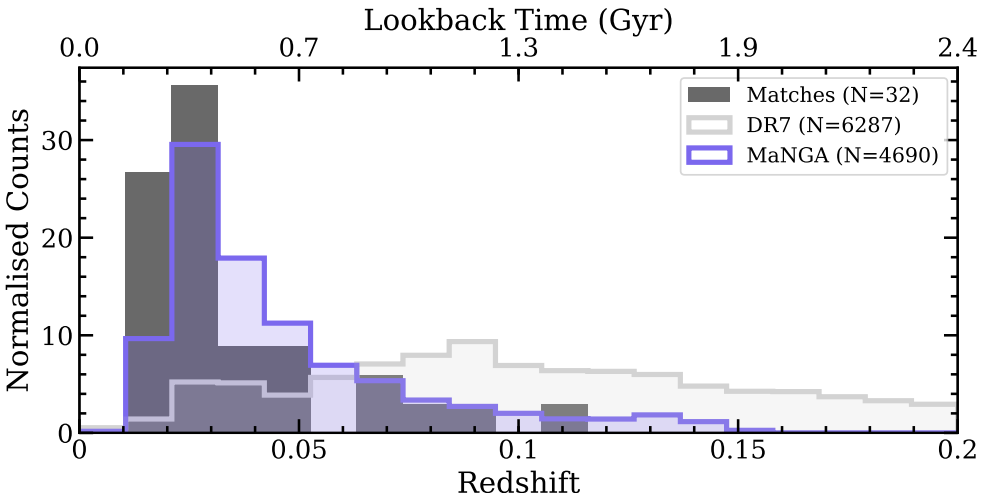

FIGURE 2.2: Redshift distribution.

2.1.1 SDSS DR7 Fibre Selected Post-starbursts

The fibre-selected post-starburst galaxies from the SDSS DR7 (Abazajian et al., 2009) are comprised of several catalogues, most notably from (Wild et al., 2010) using the Principal Component method of (Wild et al., 2007), see Sect. 2.2). They are (1) quiescent, (2) emission line, (3) AGN, and (4) dusty. The identifying characteristics of each class are discussed below.

In addition, the catalogue is made up of PSBs identified in several other catalogues, including Tremonti (unpublished; *private comm.*) and Alatalo (SPOGs; Alatalo et al. (2016)). The Tremonti method preferentially selects very young PSBs, often immediately following the starburst episode. Meanwhile, the Altalo sample of possibly shock-driven post-starburst galaxies (SPOGs) features low S/N spectra.

For typically sized galaxies within our redshift range ($0.01 < z < 0.11$), the DR7 spectra of the central 3" are highly aperture-limited to only the central $0.4 - 6.0$ kpc of galaxies, with a median redshift of 0.024 corresponding to 1.4kpc (i.e. bulge). Not only does this have the effect of smearing together the aggregate stellar populations within the aperture, but it also prevents the study of the outermost regions of the galaxy. This *aperture bias* is a known effect, and has been well-studied (e.g. Kewley et al., 2006; Gomes et al., 2016). In brief, single-fibre spectroscopic methods are not able to view the outer, starforming discs of many nearby galaxies, wrongly concluding that, viewed only by their inner AGN-dominated bulge region, such objects have already ceased star formation. This effect is strongly convolved with redshift, since the angle subtended by more distant (but still low redshift) galaxies is decreased, and hence the physical scales probed by a 3" fibre are increased. Galaxies which are undergoing inside-out quenching, as may be the case for many PSBs, are thus wrongly classified.

The following classification scheme is comprised of the six spectral classes, with 32 galaxies in our final sample. Note that some objects are selected by multiple catalogues, and hence the counts quoted below do not sum to 32 nor do the percentages (i.e. N/32) sum to unity. While the purple hexagons denote the MaNGA IFU, the white circles denote the 3" fibre aperture. The images shown demonstrate the typical features inherent to that class, as well as the overall range in morphology and angular size.

Wild - Quiescent (Wq) | N = 5 (16%)

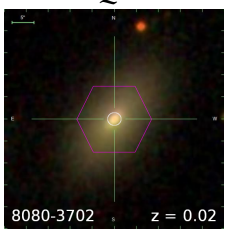

This class already has the appearance of a typical quiescent galaxy: red colours, elliptical shape, and no obvious signs of star formation. These galaxies are typical of traditional post-starburst galaxies.

Wild - Emission Line (We) | N = 4 (13%)

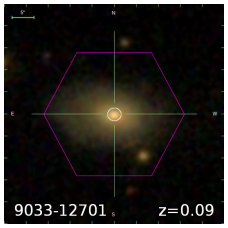

This class of PSB features strong emission lines, which indicates ongoing nebular emission. However, the Balmer absorption lines of this class are more likely to have infilling by coincident emission, which can hide the true extent of the absorption.

Wild - Active Galactic Nucleus (Wa) | N = 5 (16%)

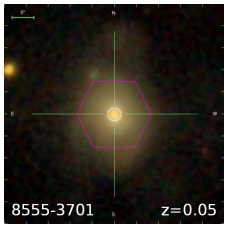

These objects feature strong emission-line ratios as determined by the strength of the ionising radiation with the central 3", which places them above the Kewley et al. (2001) AGN demarcation line.

Wild - Dusty (Wd) | N = 9 (28%)

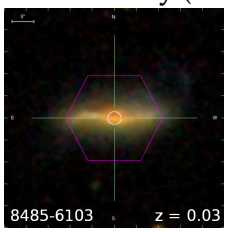

Dust is strongly correlated with molecular gas, obscuring ongoing star formation and mimicking older stellar populations. Hence, these objects may be dusty starbursts, and not bona fide PSBs.

Tremonti (T) | N = 9 (28%)

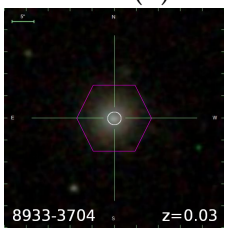

This unpublished catalogue of post-starburst candidates from SDSS DR 8 is selected on both EW($H\alpha$) and a combination of $H\delta + H\gamma$ absorption. These objects are some of the youngest post-starbursts in our sample.

Altalo/SPOG (S) | N = 6 (19%)

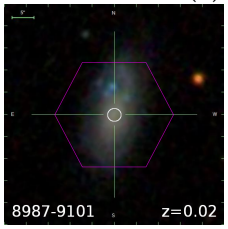

SPOGs are galaxies chosen from the Shocked POst-starburst Galaxy Survey, which identifies transforming galaxies where shocks may contribute to the nebular emission, unlike typical star-forming galaxies.

2.1.2 MaNGA Integral Field Post-starbursts

The corresponding sample as measured by the Mapping Nearby Galaxies at the Apache Point Observatory (MaNGA) MPL-6 contains spectral datacubes for each galaxy, as well as kinematic and emission-line maps. There are several different integral field unit (IFU) bundle sizes designed for flexible observation, and hence varying angular diameters subtended. The standard MPL-6 catalogue only contains maps of the stellar and gas radial and dispersion velocities, as well as some important emission lines (e.g. Hα, Hβ), and their derived quantities (e.g. EW (Hα)). We chose to adopt maps of D4000 and Hδ absorption available from the PIPE3D value-added catalogue for MPL-6 (Sánchez et al., 2016, 2018), discussed below.

The signal-to-noise (S/N) across the MaNGA field-of-view (FoV) is dependent on the brightness at that spectral pixel (spaxel), and hence deteriorates significantly at the edges of the IFU. To account for this, the stellar-continuum, and hence stellar kinematics, are measured by binning the spaxels via the Voronoi tessellation method (PPXF; (Cappellari and Copin, 2003)) with a target S/N $\sim$ 10, and modelled using the MILES spectral template library (Sánchez-Blázquez et al., 2006). However, the emission-line measurements are performed on each spaxel *without binning*. This hybrid method is extremely useful to produce stellar and emission-line maps with similar S/N. We eliminate poor quality bins according to the bitmasks provided by the MaNGA pipeline. Secondary masking is then performed specific to each map type, as described below.

Velocity Maps

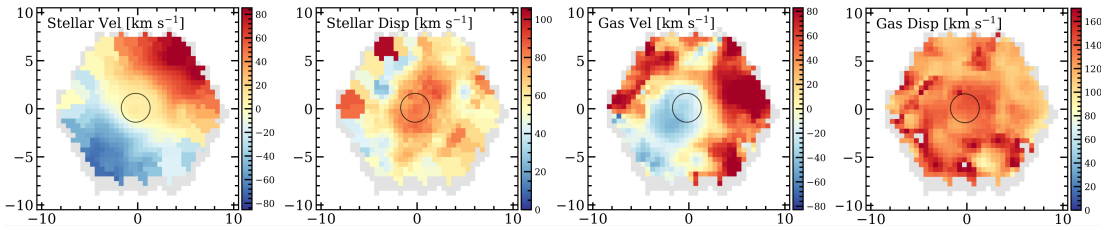

FIGURE 2.3: Stellar and gas radial velocity and dispersion maps of the object "8080-3702" calculated with PPFX. Axes are in arcsec.

Not only does the bimodality of galaxies appear in terms of morphology and colours, but it is also embedded in the kinematics. Star-forming galaxies tend to be rotationally-dominated (i.e. discy), expressed as a coherent rotational velocity pattern and with little dispersion. Quiescents tend to be the opposite: incoherent rotation with high dispersion-supported bulges. Disturbed gas patterns may indicate a recent disturbance, such as a merger event. An example of such velocity patterns is shown in Fig. 2.3.

Masking for the velocity maps is typically minimal across the sample, especially for galaxies which the MaNGA IFU does not entirely cover. Some bins are removed for contamination, and others are removed due to low S/N.

Ancillary Maps

Although the analysis of this work utilises the PCA method, a comparison to maps of traditional line-index measurements is a useful control. Of interest to the study of PSBs in particular, the D$_n$4000 and Hδ absorption indices provide useful information

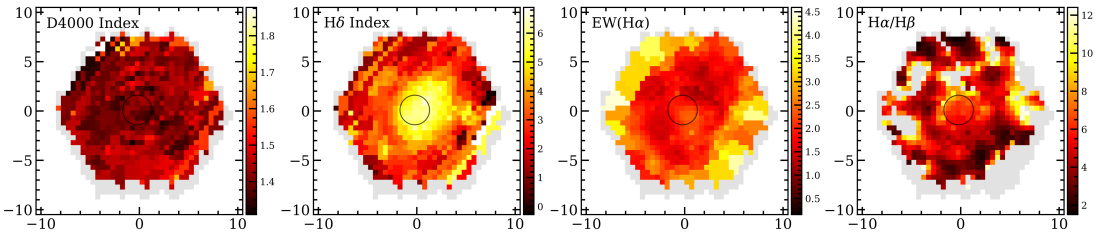

FIGURE 2.4: Ancillary maps of "8080-3702". The D4000 and Hδ indices are from `Pipe3D`, and the EW(Hα) and Hα/Hβ are from the standard MaNGA pipeline. Axes are in arcsec.

on the strength of the 4000-Å break, and the dominance of AF-type stars. D_n4000 is a similar to D4000 in that they both measure the flux ratio at the ends of the 4000-Å break, but D_n4000 adopts a narrower wavelength interval and is hence insensitive to dust. However, we are force to adopt the more dust sensitive D4000 measurements, asPIPE3D does not include D_n4000 and it is the only added-value catalogue to include all of MPL-6. In addition, EW(Hα) is an indicator of nebular emission, indicative of star-formation. Lastly, the Balmer decrement Hα/Hβ acts as a preliminary dust extinction map, as Hβ ($\lambda = 6104$Å) is preferentially extincted. An example of the ancillary maps is shown in Fig. 2.4.

Spectra

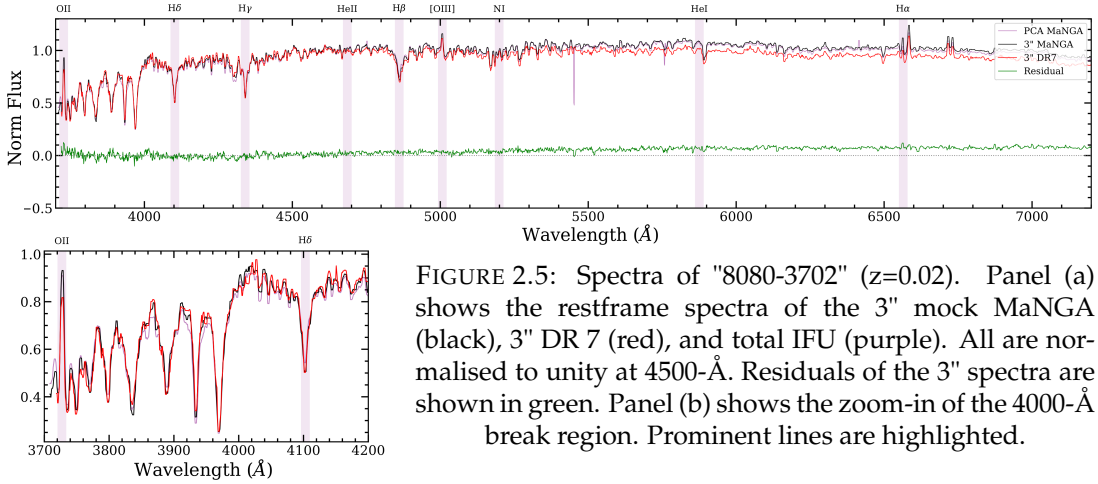

FIGURE 2.5: Spectra of "8080-3702" (z=0.02). Panel (a) shows the restframe spectra of the 3" mock MaNGA (black), 3" DR 7 (red), and total IFU (purple). All are normalised to unity at 4500-Å. Residuals of the 3" spectra are shown in green. Panel (b) shows the zoom-in of the 4000-Å break region. Prominent lines are highlighted.

In order to facilitate an equal comparison with the 3" DR7 spectra, we collapse the total MaNGA datacube to produce mock 3" spectra for each galaxy in the sample. Line-of-sight Galactic extinction due to dust is corrected in the observed frame according to Cardelli et al. (1989) and using the E(B-V) map of Schlegel et al. (1998). This step is also performed on the 3" DR 7 spectra in a consistent way. Then we shift the dust-corrected MaNGA spectra onto the a common wavelength grid in the restframe assuming the spectroscopic redshifts from MaNGA. We do not correct for the peculiar velocities arising from rotation, as the 3" DR 7 measurements are single aperture. Given that the full-width half-maximum (FWHM) of the MaNGA datacubes is ∼2.5", and that the pixel scale is 0.5"/px, the mock selection must account for the beam smearing sensitive to the 3" selection. Hence, the diameter is extendedly slightly to 3.2" for a better match in terms of absolute spectral flux. Fig. 2.5 demonstrates the agreement between the 3" DR 7 spectrum and the mock 3" MaNGA spectrum.

2.2 Principal Component Analysis

Star-formation cessation has been typically measured by Hδ absorption line index, as it is the most prominent Balmer absorption-line that is covered by a wavelength range used to probe the 4000-Å break. However, this method has been significantly limited by the high S/N required to measure Hδ accurately, leading to sample selection of only the strongest PSBs. In addition, the strength of the Hδ index is dependent on the luminosity-weighted mean stellar ages of the underlying population, and so excluding candidates with too strong Balmer line EW in absorption that limits a sample to only the youngest and strongest post-starbursts.

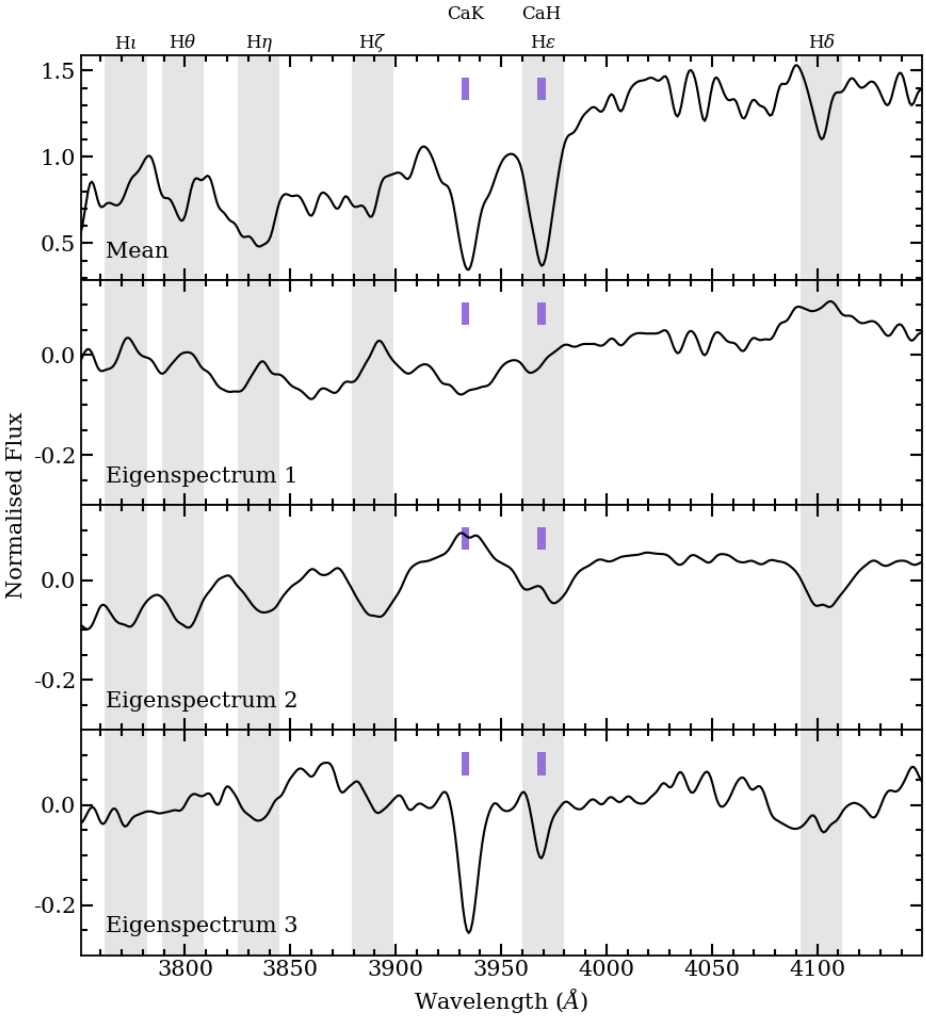

FIGURE 2.6: Mean and first three principal components from the Wild et al. (2007) eigenbasis. Balmer lines are highlighted in grey, and CaII (H&K) shown by purple dashes.

Principal component analysis (PCA) has long been applied to galaxy spectra (e.g. Murtagh and Heck, 1987; Connolly et al., 1995), as it helps to identify correlations and to emphasise the greatest variations in a given set of data. Wild et al. (2007) developed a PCA eigenbasis over 3750-4150Å based on stocastic burst models built using the GALAXEV spectral synthesis code (Bruzual and Charlot, 2003, see Sec. 2.4.1). By optimally modelling all of the Balmer emission lines at once, and by characterising their

strength with a single parameter, one can recover more accurate information than by a measurement of Hδ alone. Results show that this approach is able to probe the Balmer absorption to much lower S/N than conventional line index methods.

The first three principal components, corresponding to the first three eigenspectra shown in Fig. 2.6, are readily identifiable. PC1 measures the strength of the 4000-Å break, and is correlated to the Balmer absorption. PC2 measures the excess Balmer absorption, primarily by Hδ. PC3 measures the excess CaII (H&K) absorption. The single measurement analogues of D_n4000 and Hδ measured by PC1 and PC2, respectively, are well-studied and known to provide the greatest variation within this spectral range. The analogue CaII (H&K) is a less commonly used indicator of star-formation, but has been identified as a clear measurement of AF-type stars (Rose, 1985), and for breaking the age-strength degeneracy found for recent starbusts (Leonardi and Rose, 1996; Leonardi and Rose, 2003).

When viewed as a parameter space, the PCs of (Wild et al., 2007) allow for the PCA-derived classification of more than just post-starburst galaxies, but rather the entire range of galaxies observed. Building off this success, (Rowlands:*in prep.*) has devised a set of regions corresponding to galaxy classes: starburst, starforming, quiescent, green valley, and post-starburst. The region boundaries have been empirically calibrated using MaNGA MPL-6, as shown in the PC plane of Fig. 2.7. The regions are slightly different depending on whether the galaxy is above or below 10^{10} $M_\odot$.

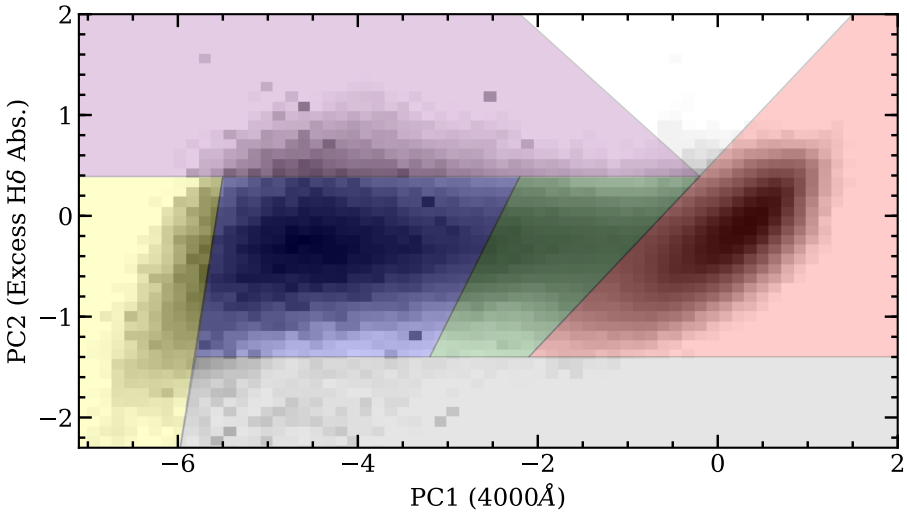

FIGURE 2.7: Distribution of the individual spaxels in MaNGA MPL-6, as measured by principal component analysis, shown in grey logscale bins. The coloured regions denote the five galaxy types: starburst (yellow), starforming (blue), quiescent (red), green valley (green), and post-starburst (purple).

This is a clear demonstration of the power of PCA over traditional colour-mass or SFR-M_* spaces in identifying galaxy types. While the blue cloud and red sequence are preserved, the transitional stages of starburst, post-starbust, and green valley are easily distinguished. As demonstrated and discussed in Pawlik et al. (2016), the leftmost side of the PC plane denotes the evolutionary pathway for a galaxy from the initial starburst episode and into the quenching PSB stage. This notion of the PC plane as an ideal parameter space to explore the timeline of galaxy evolution, and quenching in particular, will play a central role throughout the remainder of this investigation.

2.2.1 Normalised "Gappy" PCA

With the eigenbasis in hand, acquiring the principal components is straightforward. As shown by Eq. 2.1, the data **F** are modelled from an eigenbasis $\mathbf{e}_{i,\lambda}$ and corresponding amplitudes a_i, a mean spectrum $\mathbf{c}_\lambda$, and a normalisation factor N. The amplitudes a_i and normalisation factor N are simultaneously fit using the least-squares method given by Eq. 2.2. A full description of the projection methods, including intermediate equations, is provided in Appendix A.[1]

$$\mathbf{F}_\lambda = N(\mathbf{c}_\lambda + \sum_{i=1}^{n_{pc}} a_i \mathbf{e}_{i,\lambda}) \tag{2.1}$$

$$\chi^2 = \sum_\lambda \mathbf{w}_\lambda (\mathbf{F}_\lambda - N(\mathbf{c}_\lambda + \sum_{i=1}^{n_{pc}} a_i \mathbf{e}_{i,\lambda}))^2 \tag{2.2}$$

Although the data being modelled must span the wavelength vector of the eigenbasis, the method is called "gappy" as it can handle masked arrays (Lemson, *unpublished*). The level to which this masking can be applied varies with how much of the eigenbasis is considered. We find that whereas including all 440 eigenspectra can create considerable noise within the masked regions, including only the first three eigenspectra allows for a larger amount of masking as the number of degrees of freedom within the model is decreased.

2.2.2 Mapping PCA in MaNGA

Although the single-fibre PCA studies have revealed much about galaxy evolution, it is now possible to leverage the power of spatially-resolved spectroscopy to view and model variations in PC values across a single galaxy. We obtain maps corresponding to the first three principal components from (Rowlands; *private comm.*), calculated using Normalised Gappy PCA (see Sec. 2.2.1. This dataset also includes maps indicating the PC class per spaxel, corresponding to the regions from Fig. 2.7. Similar to the standard MaNGA binning scheme, these maps are binned via the Voronoi method of (Cappellari and Copin, 2003). For all the maps, we remove any bin which has $> 10\%$ fractional error measured on PC1. A sample is shown below, in Fig. 2.8.

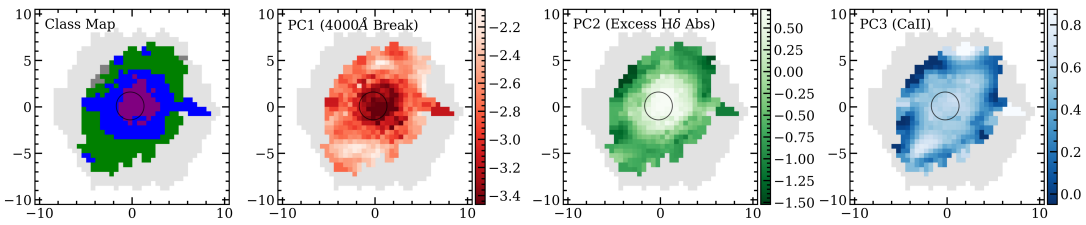

FIGURE 2.8: PCA maps corresponding to PC1 (4000-Å break), PC2 (excess Hδ absorption), PC3 (excess CaII (H&K) absorption), as well as the class map.

[1] A Python-based suite containing many of the originally IDL-only functions (incl. `GappyPCA` and `NormGappyPCA`) of (Wild et al., 2007) will be made available on Github shortly

2.3 Morphological Classification

The morphological features visible through photometry can reveal important information about a galaxy's structure, evolutionary stage, and recent merger history. Seven of the most well-studied morphological parameters are described briefly below. In general, these methods are computed over the pixels of photometric images of galaxies, such as the extensive photometric catalogue of the SDSS. All but shape asymmetry is sensitive to the band used, and hence the derived values may vary.

- n - Sérsic Index. Measures the cuspiness of the surface brightness profile. Typically $\sim$1 for starforming galaxies, and $2 < n < 4$ for quiescents (Sérsic, 1963).
- C - Concentration. Measures the ratio of the growth curve radii at 20% and 80% of the total light. Lies between 2 and 5, favouring quiescent galaxies for $C \gtrsim 4$ and starforming $\sim$3 (Bershady et al., 2000), (Conselice, 2003), (Hernández-Toledo et al., 2008).
- A - Asymmetry. Measures the flux of one pixel rotated 180° about the centroid that minimises A, compared to the flux of the un-rotated pixel. The values are normalised and background subtracted. Starforming galaxies have $A \sim 0.1$, while quiescents have $A \sim 0.2$ (Conselice et al., 2000), (Conselice, 2003), (Hernández-Toledo et al., 2008).
- S - Clumpiness. Measures the pixel intensity for a suitably Gaussian smoothed image, relative to the un-smoothed pixel at the same position. Lies in the range of 0.1-0.3, and tends to be greater for starforming galaxies (Isserstedt and Schindler, 1986; Takamiya, 1999; Conselice, 2003).
- G - Gini Index. Measures the degree of inequality of light across a galaxy, independent of the centrality of the nucleus. Values typically lie around $G \sim 0.6$ for quiescents, and ~ 0.4 for starforming (Abraham et al., 2003; Lotz et al., 2004).
- M_{20} - Moment of Light. Measures the second order moment of the flux-weighted spatial extent of the brightest region of the galaxy, containing 30% of the light. Quiescents typically have low valus < -2.0, and starforming -1.5 (Lotz et al., 2004).
- A_S - Shape Asymmetry. Measures the prominence of low surface-brightness tidal features, by performing the Asymmetry calculation on un-weighted binary masks. Disturbed galaxies typically have $A_S > 0.2$ (Pawlik et al., 2016).

To characterise our sample, we acquire from (Pawlik; *private comm.*) the values of these seven parameters for the 47% of galaxies within our sample which have been observed by MPL-5[2].

[2] A more complete study which includes the total MPL-6 sample is planned.

2.4 Stellar Population Synthesis

The ability to create realistic spectral energy distributions (SED) of entire galaxies has provided a revolution in how galaxies are analysed and understood. They involve all aspects of stellar and nebular astrophysics, including dust grain chemistry. The evolutionary steps taken to transform raw stellar astrophysics into these accurate SEDs is called Stellar Population Synthesis (SPS). There are several SPS recipes available, with varying strengths and weaknesses. This work uses two common packages, which are briefly discussed in the following sections: (1) Galaxy Spectral Evolution Synthesis, and (2) Flexible Stellar Population Synthesis.

The root of all SPS is the Single Stellar Population (SSP). SSPs are composed a single co-evolving stellar population of a common metallicity and abundance pattern, evolved through time. The construction of an SSP begins with an initial mass function (IMF; Salpeter, 1955; Kroupa, 2001; Chabrier, 2003), a large range of stellar spectra (e.g. Le Borgne et al., 2003; Sánchez-Blázquez et al., 2006), and theoretical isochrone tracks (e.g. Bertelli et al., 1994). The IMF can be chosen from a handful of recipes, and governs in what proportion the stellar spectra are stitched together. The new population is then evolved according to the isochrone tracks.

The SSP provides a good starting point. However, it does not fully reproduce a realistic galaxy SED, even in a starburst. To better approach a realistic SED, secondary components such as attenuation by dust, nebular emission, and star formation history must be included. The entire set of ingredients then form a Composite Stellar Population (CSP), which can begin to reproduce realistic models. This process is illustrated in Fig. 2.9.

This being said, there are several well-known caveats to SPS. Firstly, many popular stellar population models do not include advanced prescriptions for difficult aspects of stellar evolution such as the fraction of binary stars, convection, and mass-loss. For example, the inclusion of stellar rotation has a strong effect on the relative fraction of blue and red supergiants (Maeder and Meynet, 2000, 2012). These uncertainties can strongly affect the mass-to-light ratio of their resulting SEDs. Secondly, theoretical stellar libraries (e.g. Westera et al., 2002), while providing excellent spectral sampling, are prone to incomplete prescriptions for the atomic and molecular physics. Meanwhile, empirically calibrated stellar libraries (e.g. **?**), while providing true atomic and molecular physics, are not well sampled across the HR-diagram, and are severely lacking in several important, but short-lived populations such as thermally-pulsating AGB (TP-AGB) stars. Lastly, the well-known age-metallicity degeneracy remains unresolved. Young stars are made redder since increasing metallicity increases the opacity. Older stars also have redder spectra, but lower metallicities. Hence, the spectrum of a high metallicity, young population can appear nearly identical to that of a lower metallicity, older population.

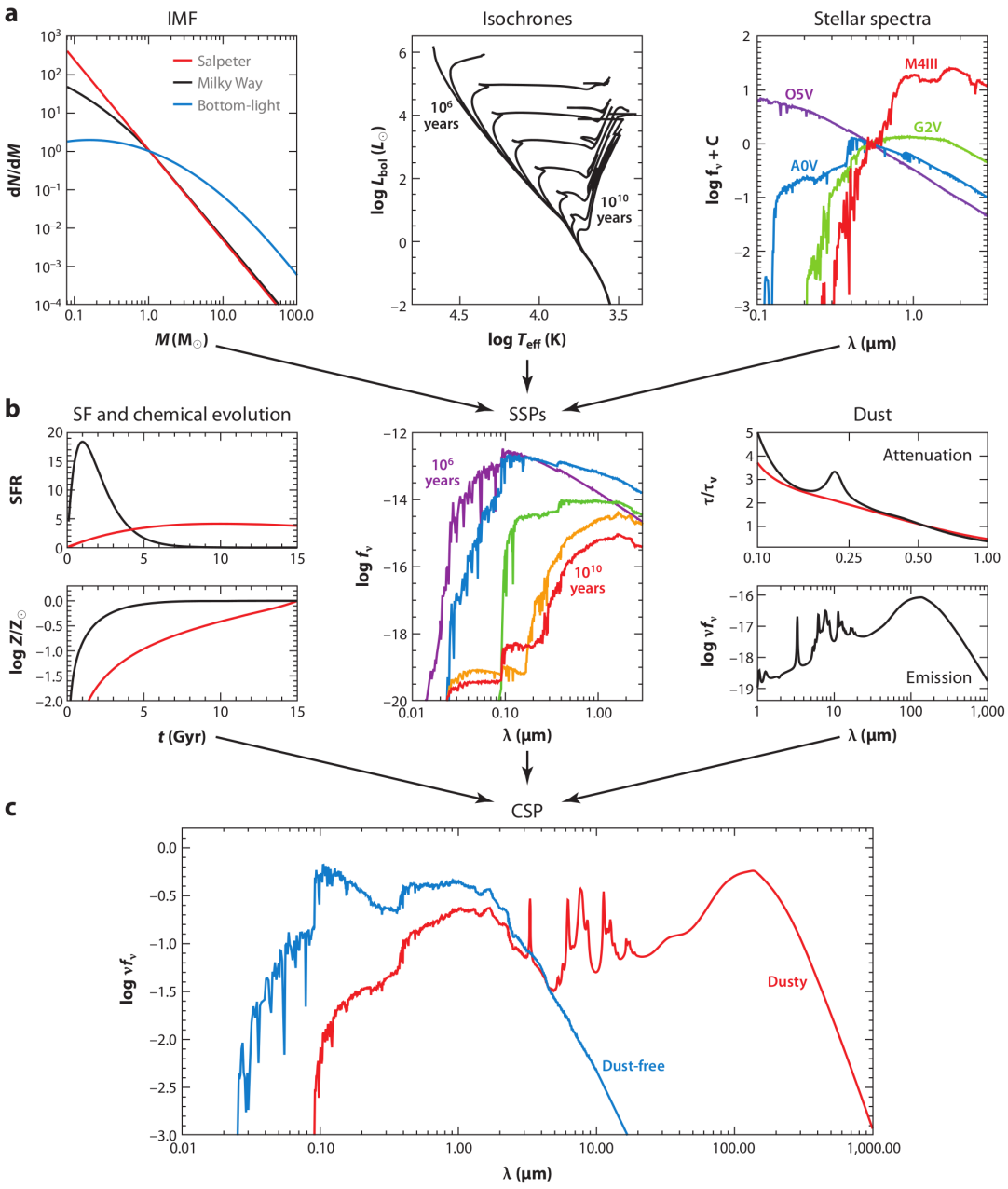

FIGURE 2.9: Summary of the spectral population synthesis method. (a) Simple stellar populations are constructed from an initial mass function, isochrone tracks across metalliticies, and a wide range of stellar spectra. (b) Composite stellar populations continue by involving star-formation histories, chemical evolution, and dust. (c) The final SED with and without dust. Figure adapted from (Conroy, 2013).

2.4.1 Galaxy Spectral Evolution Library

The Galaxy Spectral Evolution Library (GALAXEV; Bruzual and Charlot, 2003) (BC03 hereafter) is a well-known, mature SPS code which has enjoyed considerable use in the past two decades. It uses the same essential framework as described above, and uses the BaSeL theoretical library of Westera et al. (2002) and the observational STELIB library of Le Borgne et al. (2003). As of 2016, BC03 has been updated (Charlot; *unpublished*) to include the modern MILES (Sánchez-Blázquez et al., 2006) empirically calibrated stellar library. We adopt this particular library corresponding to solar metallicity and the IMF of Chabrier (2003) for use in this work.

2.4.2 Flexible Stellar Population Synthesis

The Flexible Stellar Population Synthesis code (FSPS; Conroy, 2013) gains its advantage by allowing maximal control over essential parameters such as the choice of isochrones and IMF. In addition, FSPS provides the ability to weight the various stages of stellar evolution, including the TP-AGB and horizontal branches in particular. While BC03 fails to model the far-ultraviolet, this flexibility allows FSPS to fit the whole range of ultraviolet data extremely well. FSPS can also reproduce the mainstream optical and near-IR colours of PSBs. For consistency, we adopt here the same MILES spectral template library and Chabrier IMF.

2.4.3 SPS and Post-starbursts

As discussed in Conroy et al. (2009), the models of BC03 and FSPS fail in several ways highly relevant to PSBs: photometric *ugr* colours are too red, D4000 too strong, and Hδ too weak when compared to massive quiescents. This can be explained by uncertainties in the less abundant populations of metal-poor stars, young stars, blue stragglers, and possibly bluer horizontal branch stars. It cannot, however, be explained by issues arising from treatments of stellar atmospheres or well-populated evolutionary phases. Hence, a major step forward will be made by better sampling the metallicity-age plane with improved studies of stellar clusters, and in greater number.

Although there are several key areas of improvement, SPS provides the most accurate models available for the study of extragalactic astrophysics and the evolution galaxies. For a more in-depth discussion, see the review by Conroy (2013).

3 Results

3.1 Morphologies

It has long been demonstrated that galaxy interactions and mergers can drive strong starbursts. Major merger remnants may contribute to a significant fraction of the strongest global post-starbursts observed today (Liu and Kennicutt, 1995). Minor mergers too can drive starbursting episodes, particularly in the nuclear regions where the disrupted gas can lose angular momentum and quickly accumulate (Mihos and Hernquist, 1994). Signatures of recent merger events can remain for several Gyr embedded in kinematics (Cox et al., 2006). Although morphological signatures tend to dissipate over shorter timescales, they are extremely useful in identifying disturbances.

As shown in Fig. 3.1 and summarised in Table 3.1, we examine the correlation between the seven morphological parameters discussed in Sec. 2.3 for our sample of 15 MPL-5 galaxies. The plotting windows are set to match Figure 4 of Pawlik et al. (2016). In this instance, we do not copy objects with multiple parent catalogues into separate classes. Hence, the only classes with multiple objects in MPL-5 are (1) dusty, and (2) SPOGs. As a note of caution, the asymmetries appear to be systematically lower than other control samples.

In our sample, dusty galaxies tend to have concentrations similar to starforming galaxies, clumpiness, Gini index, M_{20}, and Sérsic index are more similar to quiescents. SPOGs appear to be remarkably similar. All classes tend to have quiescent-like clumpiness and Gini index. While concentration values are significantly increased for emission-line and AGN classes, similar to quiescents, the actual quiescent class features only moderately increased concentration, although still similar with the quiescent population. Only emission-line and quiescents have values of M_{20} consistent with the quiescent population, and all but the Tremonti and SPOG classes show distinctly quiescent Sérsic indices. With the noted exception of the AGN class, the sample does not look particularly disturbed, according to shape asymmetry.

This mixture of quiescent- and starforming-like morphological parameters may indicate that this sample is indeed undergoing morphological change. This is clearly shown by the two most populated classes in our sample: dusty galaxies and SPOGs. We find good agreement with Pawlik et al. (2018) in that the AGN and quiescent classes have similar morphologies. However, unlike the large sample sizes of Pawlik et al. (2016), not much more can be learned with such low number statistics. Trends which hold up in aggregate are simply not robust to individual objects. The addition of 17 objects via MPL-6 will allow for a clearer interpretation of the range in morphologies present in our total sample.

Class	N	C	A	S	Gini	M_{20}	n	A_S
Wd	5	$2.83^{+0.77}_{-1.58}$	$0.06^{+0.06}_{-0.07}$	$0.11^{+0.06}_{-0.04}$	$0.62^{+0.1}_{-0.08}$	$-1.60^{+1.0}_{-0.59}$	$2.62^{+2.66}_{-1.34}$	$0.13^{+0.03}_{-0.04}$
We	1	4.16	0.05	0.07	0.71	-2.49	3.44	0.13
Wa	1	4.4	0.23	0.14	0.62	-1.16	4.59	0.5
WaT	1	4.12	0.03	0.07	0.72	-2.41	2.85	0.22
Wq	1	3.41	0.06	0.07	0.72	-2.28	2.6	0.11
WqT	1	2.88	0.05	0.12	0.49	-2.0	2.94	0.09
T	1	2.66	0.02	0.17	0.49	-1.89	1.37	0.18
S	4	$3.14^{+0.34}_{-0.54}$	$0.04^{+0.02}_{-0.01}$	$0.19^{+0.06}_{-0.04}$	$0.52^{+0.04}_{-0.03}$	$-1.67^{+0.35}_{-0.26}$	$1.75^{+0.73}_{-0.66}$	$0.19^{+0.08}_{-0.1}$

TABLE 3.1: Summary of the mean morphological values for each galaxy class, distinguishing objects contained within multiple catalogues. The range of maximum and minimum, relative to the mean, is shown for two classes with multiple objects.

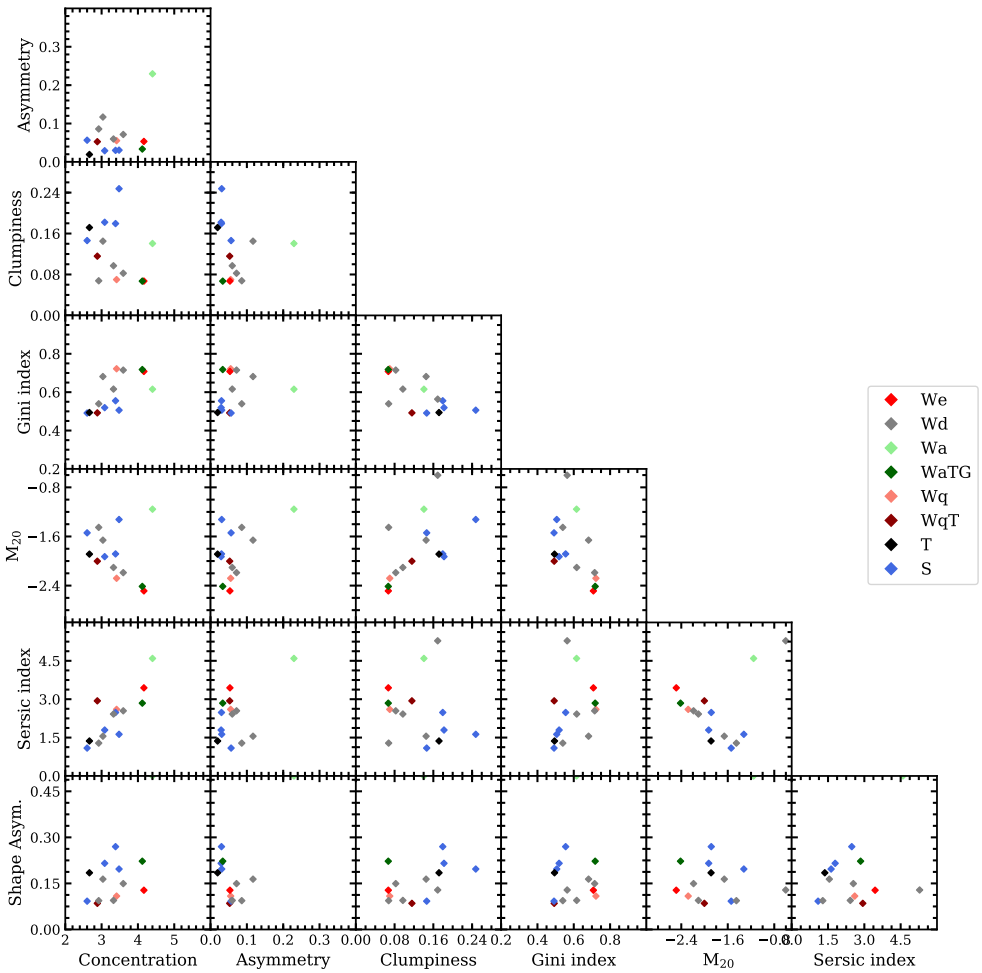

FIGURE 3.1: Summary of seven key morphological parameters: Concentration, Asymmetry, Clumpiness, Gini index, M_{20}, and Sérsic index. The points are coloured according to their DR 7-selected galaxy classes.

3.2 Aperture effects

This sample is well-suited to perform a direct comparison between the 3" aperture DR 7 spectra and the full aperture MaNGA spectra. We compute the first three principal components of spectra corresponding to the 3" DR 7, mock 3" MaNGA, and total MaNGA aperture for each galaxy in our sample, using the `NormGappyPCA` method described in Sec. 2.2.1.

An example demonstrating the subtle difference between the three spectra is given by the object "8080-3703" in Fig. 3.2. The strength of the 4000-Å break for the example object "8080-3702" is slightly lower for the 3" spectra. As well, there is significantly more absorption by Hδ for the 3" spectra. These two key differences are conveyed more succinctly in the first two principal components. This strongly suggests that the population in the outer regions is older than that within the inner 3" (1.2 kpc at $z = 0.2$), consistent with a radial gradient, and discussed in greater detail in Sec. 3.3.

We then consider the aggregate sample in-depth. As shown by Fig. 3.3, the locations of each object in the PC plane are compared between the three spectra. Panel (a) illustrates the importance of systematics between the two surveys, as some objects feature significantly different classifications. While some objects near the PSB and starforming boundary are relatively consistent, others are not. In particular, the several objects high in PC2 in DR 7 are even higher in the mock 3" MaNGA spectra. This highly incoherent pattern complicates the interpretation of panel (c), as the uncertainties in the systematics make an equal comparison between the surveys difficult. Fortunately, panel (d) is not affected by systematics between the surveys, and demonstrates that for a majority of objects, the integrated light is far less of a PSB than for the 3" center, consistent with radial gradients. However, for some objects such as SPOGs and dusty PSBs, there is very little change, suggesting that the properties of the central 3" are representative of the global population. Although a further study is out of the scope of this investigation, we emphasise that this aperture bias is strongly dependent on redshift. For clarity, panel (b) is included to summarise the locations of all 32 galaxies as seen through the total MaNGA aperture.

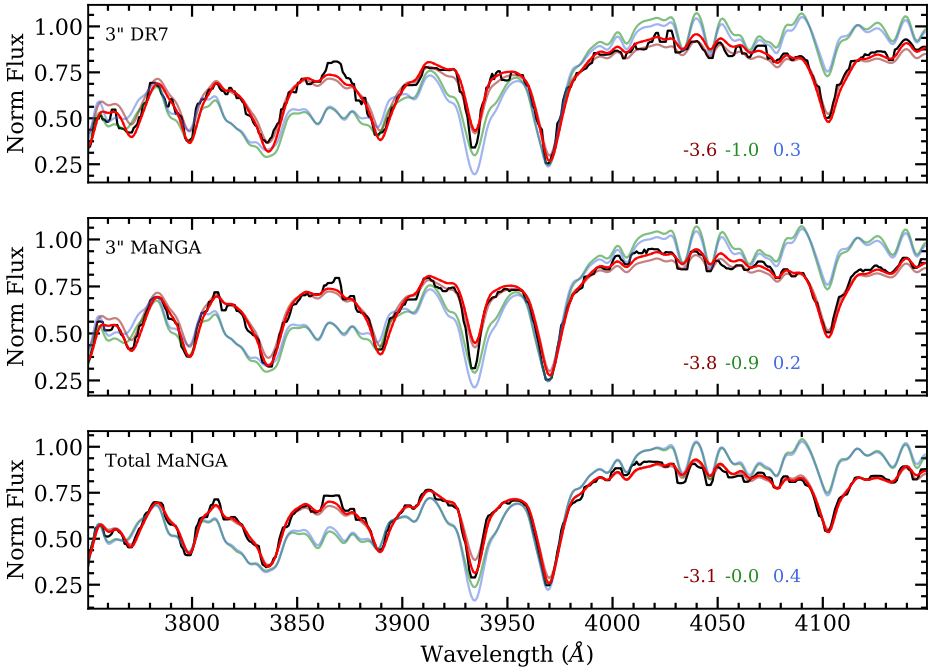

FIGURE 3.2: Reconstruction of the 3" DR7, mock 3" MaNGA, and total MaNGA spectra for object "8080-3702". Data (black) are fitted with the model (red) reconstructed using the `NormGappyPCA` method described in Sec. 2.2.1. The eigenspectra corresponding to PC1 (red), PC2 (green), and PC3 (blue) are shown, along with their amplitudes.

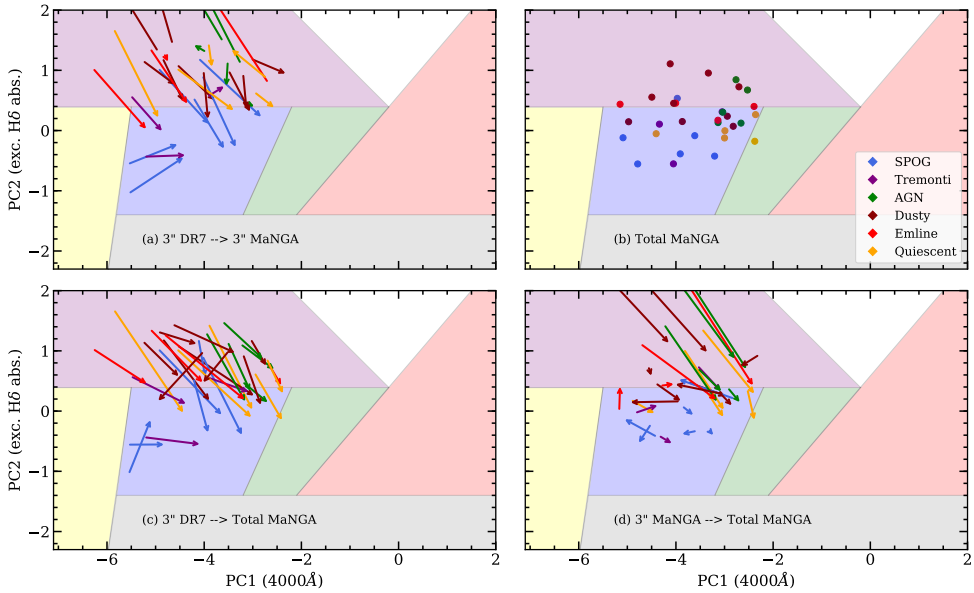

FIGURE 3.3: Aperture bias for this sample as seen with PCA. Shown in the panels are the relative positions in PC space for the spectra of (a) 3" DR 7 to the mock 3" MaNGA, (b) 3" DR 7 to the total MaNGA aperture, and (c) the mock 3" MaNGA to the total MaNGA aperture. The arrows are coloured according to class.

3.3 Radial gradients

Star formation cessation in galaxies is thought to occur on rather short timescales $\sim 3-4\,\mathrm{Gyr}$, and are hence rare events. However, the prevalence of radial gradients has shown a way forward. By understanding how the star formation cessation proceeds, we may elucidate the nature of quenching.

We consider two hypotheses:

1. There was a single burst of fixed strength in the outskirts, moving inward at later times.
2. There was a coeval starbust of varying strengths.

The first hypothesis is the more simple of the two. It supposes that the star formation in a galaxy is quenched from the outside-in. If true, then galaxies should begin to look like redder populations in the outer edges, leaving the inner disc to be quenched last. In addition, several studies have found the opposite effect of inside-out quenching, and its prevalence in large samples (Tacchella et al., 2017).

In contrast, the second hypothesis is considerably more complicated, and has a much larger parameter space to explore. It allows for different regions to starburst with different intensity, owing to the non-uniformity in the distribution and abundance of molecular gas. A larger reservoir of gas may prolong star formation, elongating the quenching timescale significantly.

Now with integral field methods, it is possible to examine models of galaxy evolution in the context of spatially-resolved radial gradients. PCA further improves the situation by decreasing the S/N floor available to be probed, hence increasing accuracy and sample size. Here we attempt to use varying SPS models of star formation cessation to better understand the radial gradients in our sample, as indicated by the strength of the 4000-Å break (PC1) and excess Balmer absorption (PC2).

We construct model grids by varying the burst-mass fraction, measured as the fraction of mass of the underlying population expressed in the burst. The evolution of a single model assumes the first hypothesis, whereas evolution at a fixed age with varying burst-mass fraction assumes the second hypothesis. Hence the evolution of PSBs may be elucidated by comparing the grid structure to the radial gradients.

Models are constructed for both BC03 and FSPS, assuming a strong, short-lived burst at $t = 0$. The remaining evolution is entirely passive. We vary the spectrum used for the background population according to six different models:

- A single empirical elliptical spectrum
- Single-burst quiescent at $t = 0$ sampled at 13 Gyr from BC03
- Galaxy with a constant SFR sampled at 13 Gyr from BC03
- Median-stacked quiescent galaxy from MPL-6
- Median-stacked starforming galaxy from MPL-6
- Median-stacked green valley galaxy from MPL-6

The effect of the underlying population becomes visible once the burst subsides, and strongly affects where in the PC plane the galaxy will ultimately reside. This feature demonstrates the limitations of such a 'toy' model as there is evidence which suggests

that PSBs descend from star-forming galaxies, and quench (either directly or over a series of bursts) to become an elliptical - which these models are unable to reproduce. Thus, while they are useful at examining the burst behaviour at the current epoch, these models are less helpful in predicting the ultimate fate of a particular galaxy.

With this in mind, we present a few of the model grids overlaid on the object "8440-6104" in Fig. 3.4. Age increases along the set of solid lines, one for each burst mass fraction from 0.01% to 10% of the total background galaxy stellar mass. The dotted lines are drawn at constant age. The locus of each radial grid is plotted in grey to guide the eye. No other underlying population fits this particular data well, but this is not the case for all objects.

The two SPS codes can be compared between panels (a) and (b), where the burst occurs over a green valley population. Firstly, the starting locations are not consistent. However, this is due to the exact shape of the progenitor burst. While BC03 can produce an easily interpretable tophat burst, FSPS is unable to do so, and is substituted here with a similar exponentially decreasing SFR. However, the models become consistent within 0.5 Gyr. At this stage, the second point becomes apparent: while FSPS overturns quickly once inside the PSB region, BC03 overshoots PC2 significantly. This in turn affects evolution later than 1 Gyr, as the angle of approach to the green valley is steeper for BC03. The third point continues on in that the end-stages as modelled with FSPS do not converge and hence do not share the same luminosity, as is the case with BC03. Panel (c) demonstrates point four: the choice of underlying population does not only affect the end location, but it also affects the grid density at later times. This results in a strong degeneracy between the single-burst and coeval hypotheses. If this is a realistic evolutionary track for PSBs, then it may only be possible to distinguish these two hypotheses for the very youngest post-starbursts.

Notwithstanding the differences between these two models, it is important to note the fantastic agreement between the grids assuming a green valley population and the locus of the radial gradient. The quiescent grid in panel (c) also reproduces the locus, although to a much lesser extent. This particular set of tracks suggests that this object has evolved for 0.4-0.5 Gyr following a coeval burst of star formation of varying strengths (i.e. hypothesis two). Although the degeneracy is significant, these tracks may even suggest that the outermost 4" of the aperture evolved according to hypothesis one.

However, this is the interpretation of a single object. The sample as a whole features some galaxies which are also well-matched by certain tracks. Interestingly, there are several galaxies whose radial gradients have a kink. The inner regions of the gradient are fit best by a coeval burst, and the outer regions by a radially evolving burst (see '8080-3704'). In addition, some objects appear to have larger burst mass fractions in the outermost regions, counter to the majority of the sample (see '8547-12705', '8485-6103'). None of these outlier objects are identified by a single class, highlighting the considerable complexity in understanding post-starbust (and likely post-merger) galaxies.

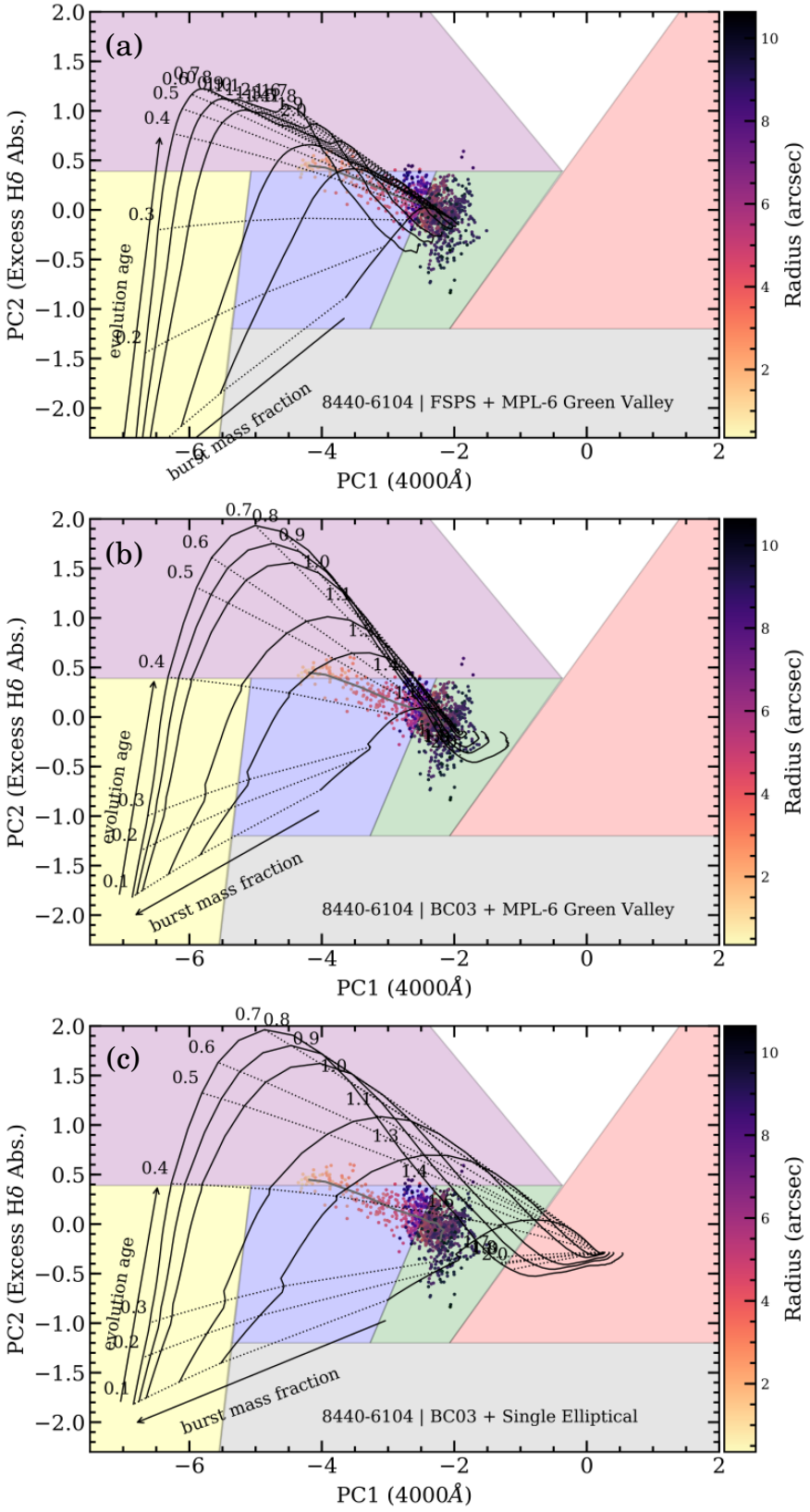

FIGURE 3.4: Examples of evolutionary tracks for "8440-6104". Points corresponding to individual spaxels are coloured by radius, with the locus overlaid in grey. Model tracks increasing in burst mass fraction from 0.01% to 10% are shown in solid black, with lines at fixed ages are shown in dotted black. Ages are marked in Gyr.

4 Conclusions

We have presented a series of analyses on 32 fibre-selected post-starburst galaxies observed with both 3" SDSS DR 7 single fibre spectroscopy and MaNGA integral-field spectroscopy. The sample has already been well-studied in the DR 7, which provides information on the character of each post-starbust. The spatially-resolved MaNGA standard and ancillary maps allow a deep probe of the velocities and spectral features. We employ a principal component analysis in identifying the strength of the 4000-Å break and excess Balmer absorption. Our main results are as follows:

- Our sample displays diverse morphologies, as measured with the morphological parameters concentration, asymmetry, clumpiness, Gini index, Sérsic index, and shape asymmetry. We demonstrate the correlation between these parameters, and briefly discuss the the particular morphologies found for different classes of objects. The sample does not look significantly disturbed, and if the indeed mergers are a significant route to quiescence, then the combination of starforming- and quiescent-favoured parameters for a given object suggests ongoing evolution.
- Our sample is well-suited to examine the effects of aperture bias. We compare the locations in the PC1/PC2 plane as measured by the 3" DR 7 spectra, mock 3" MaNGA spectra, and the total MaNGA aperture. We find significant systematics between the 3" spectra. However, a direct comparison between the mock 3" MaNGA spectra and the total MaNGA aperture reveals a trend away from post-starburst classification, and towards the main sequence, consistent with radial sSFR gradients.
- The primary objective of this work has been to examine the radial sSFR gradients within this sample by comparing to a diverse set of models. A short-burst SFH is ascribed to a set of underlying populations, which is then evolved according to the prescriptions of BC03 (Bruzual and Charlot, 2003) and FSPS (Conroy et al., 2009; Conroy and Spergel, 2011). The model tracks, varied in burst-mass fraction, are complex. Their end locations are also strongly dependent on the choice of underlying population. We find good agreement in terms of the age progression at the onset of the post-starburst phase, but differences in the peak values of PC2, and end stage burst luminosities. Despite these systematics, the result is a remarkable agreement between the evolutionary tracks and the majority of the radial gradients found within this sample.
- We also provide a suite of tools following the GAPPYPCA package of Wild et al. (2009), specifically for PYTHON users. The structure of the method is presented in Appendix A, and available on Github shortly.

Further work on this peculiar and interesting set of low-redshift post-starburst galaxies is ongoing. The completion of MaNGA, and the first light of new integral field surveys, will provide an extensive dataset with which to study this population of transitioning galaxies and to elucidate the nature of galaxy bimodality and the cessation of star-formation.

4.1 Final Thoughts

These galaxies display a range and complexity which makes their study challenging. It has been fortunate that massively multiplexed integral-field spectrographic surveys have provided new channels through which to explore these spatially- and spectrally-resolved components of these objects. However, it is our understanding of the underlying stellar and gaseous components which holds us back. Improvements to the theoretical models of stellar population synthesis, particularly in widening the age-metallicity space currently observed, and more complete prescriptions to galaxy simulations (zoom-in as well as cosmological volume) will no doubt increase confidence in these models. As well, an increased understanding in the physics of star formation on galaxy-wide scales, its role in galaxy evolution, and dependence on redshift will provide a critical test bed for SPS. The combination of these efforts will no doubt yield new and unexpected results.

A Normalised Gappy PCA

Masked spectra are often the root of difficulty when it comes to astrophysical modelling. Building on the success of principal component analysis (PCA), Connolly et al. (1995) showed that a "gappy" PCA is possible. This method is also motivated by normalisation concerns, as incoming spectra are often from different datasets than the eigensystem of the PCA.

Here we present the formal mathematical process which underlies a principal component reconstruction for a given dataset using a normalised "gappy" PCA:

The model, given by Eq. A.1, aims to fit the normalisation parameter N and PCA amplitudes a_i simultaneously. The eigenspectra are given by $\mathbf{e}_{i,\lambda}$, and the mean array for the eigenspectra is given by $\mathbf{c}_\lambda$.

$$\mathbf{F}_\lambda \;=\; N(\mathbf{c}_\lambda + \sum_{i=1}^{n_{pc}} a_i \mathbf{e}_{i,\lambda}) \tag{A.1}$$

The solution is then determined by a least squares minimisation procedure, given by Eq. A.2, which is solved by Eq. A.3. $\mathbf{w}_\lambda$ are the weights ascribed to the data.

$$\chi^2 \;=\; \sum_\lambda \mathbf{w}_\lambda (\mathbf{F}_\lambda - N(\mathbf{c}_\lambda + \sum_{i=1}^{n_{pc}} a_i \mathbf{e}_{i,\lambda})^2 \tag{A.2}$$

$$\mathbf{F}_\mu - N\,M - N \sum_{i=1}^{n_{pc}} a_i \mathbf{e}_{i,\lambda} = 0 \tag{A.3}$$

The components are given by $\mathbf{F}_c$, M, and $\mathbf{E}_i$.

$$F_c := \sum_\lambda \mathbf{w}_\lambda \mathbf{F}_\lambda \mathbf{c}_\lambda$$

$$M := \sum_\lambda \mathbf{w}_\lambda \mathbf{c}_\lambda^2$$

$$\mathbf{E}_i := \sum_\lambda \mathbf{w}_\lambda \mathbf{e}_{i,\lambda} \mathbf{c}_\lambda$$

Now we calculate the weighting array $\mathbf{M}_{ik}$, and the weighted data array $\mathbf{F}_k$, in order to form the second equation (Eq. A.4) to solve for N and a_i for the K^{th} eigenspectrum.

$$F_k := \sum_\lambda \mathbf{w}_\lambda \mathbf{F}_\lambda \mathbf{e}_{k,\lambda}$$

$$M_{ik} := \sum_{\lambda} \mathbf{w}_{\lambda} \mathbf{e}_{i,\lambda} \mathbf{e}_{k,\lambda}$$

$$\mathbf{F}_k - N\,\mathrm{E}_k - N \sum_{i=1}^{n_{pc}} a_i \mathbf{M}_{ik} = 0 \tag{A.4}$$

We form Eq. A.5 by combining Eq. A.3 and Eq. A.4:

$$(A.3) \times \mathbf{F}_k - (A.4) \times F_{\mu} \rightarrow F_{\mu}\mathbf{E}_k - M\,\mathbf{F}_k + \sum_{i=1}^{n_{pc}} a_i (F_{\mu}\mathbf{M}_{ik} - \mathbf{E}_i\mathbf{F}_k) = 0 \tag{A.5}$$

Update $\mathbf{M}_{ik}$ and $\mathbf{F}_k$ to account for normalisation:

$$\tilde{\mathbf{M}}_{ik} := F_{\mu}\mathbf{M}_{ik} - \mathbf{E}_k\mathbf{F}_i$$

$$\tilde{\mathbf{F}}_k := M\mathbf{F}_k - F_{\mu}\mathbf{E}_k$$

Finally, we obtain the principal components a_i and corresponding normalisation N.

$$a_i = \sum_{k} \tilde{\mathbf{M}}_{ik}^{-1} \tilde{\mathbf{F}}_k$$

$$N = F_{\mu} / (M + \sum_{i} a_i \mathbf{E}_i)$$

Reconstruction is straight-forward, and follows from the model presented in Eq. A.1.

B Extended Results

Due to the the intermediate sample size presented here, it is impractical to supply all of the figures related to this analysis. However, given it may be of interest to examine objects, spectra, and models individually, we supply the extended results via www.st-andrews.ac.uk/j̃rw20/results/

B.1 MaNGA Maps

A master .pdf document containing the following for the entire sample of 32 objects:

- post-stamp image with MaNGA IFU indicated
- Important metrics (RA, Dec, z, etc.)
- Morphological parameters [MPL-5 ONLY]
- PC Plane with radial gradient overlaid
- PCA Maps: class, PC 1-3
- Kinematics: stellar and gas radial velocity and dispersion
- Auxiliary: D4000, Hδ absorption, EW (Hα), and Hα/Hβ
- Overlaid spectra (3" DR 7, mock 3" MaNGA; total aperture MaNGA), residuals, and 4000-Å zoom-in

B.2 Spectra

A master .pdf document containing overlaid spectra (3" DR 7, MaNGA; total MaNGA), residuals, and 4000-Å zoom-in. Also includes mean spectra for the sample of 32, overlaid.

B.3 Model Grids

A directory containing 12 model grids per object (6$\times$ for both BC03 and FSPS).

- Ellip - Single elliptical galaxy
- KR(GV/Q/SF) - MPL-6 median stack green valley, quiescent, and starforming
- BC(Q/SF) - BC03 end-state spectra for a single burst, and constant SFR

Bibliography

Abazajian, K. N., Adelman-McCarthy, J. K., Agüeros, M. A. et al. (2009), 'The Seventh Data Release of the Sloan Digital Sky Survey', *The Astrophysical Journal Supplement Series* **182**.

Abraham, R. G., van den Bergh, S. and Nair, P. (2003), 'A New Approach to Galaxy Morphology. I. Analysis of the Sloan Digital Sky Survey Early Data Release', ApJ **588**, 218–229.

Alatalo, K., Cales, S. L., Rich, J. A. et al. (2016), 'Shocked POststarbust Galaxy Survey. I. Candidate Post-starbust Galaxies with Emission Line Ratios Consistent with Shocks', *The Astrophysical Journal Supplement Series* **224**.

Arnouts, S., Walcher, C. J., Le Fèvre, O. et al. (2007), 'The SWIRE-VVDS-CFHTLS surveys: stellar mass assembly over the last 10 Gyr. Evidence for a major build up of the red sequence between z = 2 and z = 1', *Astronomy and Astrophysics* **476**, 137–150.

Astropy Collaboration, Robitaille, T. P., Tollerud, E. J. et al. (2013), 'Astropy: A community Python package for astronomy', A&A **558**, A33.

Bacon, R., Accardo, M., Adjali, L. et al. (2010), The MUSE second-generation VLT instrument, *in* 'Proceedings of the SPIE, Volume 7735, id. 773508 (2010).', Vol. 7735.

Baldry, I. K., Balogh, M. L., Bower, R. G. et al. (2006), 'Galaxy bimodality versus stellar mass and environment', *MNRAS* **373**, 469–483.

Baldry, I. K., Glazebrook, K., Brinkmann, J. et al. (2004), 'Quantifying the Bimodal Color-Magnitude Distribution of Galaxies', *Astrophysical Journal* **600**, 681–694.

Barro, G., Faber, S. M., Koo, D. C. et al. (2017), 'Structural and Star-forming Relations since z 3: Connecting Compact Star-forming and Quiescent Galaxies', ApJ **840**.

Belfiore, F., Maiolino, R., Maraston, C. et al. (2016), 'SDSS IV MaNGA - spatially resolved diagnostic diagrams: a proof that many galaxies are LIERs', MNRAS **461**, 3111–3134.

Bell, E. F., Wolf, C., Meisenheimer, K. et al. (2004), 'Nearly 5000 Distant Early-Type Galaxies in COMBO-17: A Red Sequence and Its Evolution since z˜1', *Astrophysical Journal* **608**, 752–767.

Bershady, M. A., Jangren, A. and Conselice, C. J. (2000), 'Structural and Photometric Classification of Galaxies. I. Calibration Based on a Nearby Galaxy Sample', AJ **119**, 2645–2663.

Bertelli, G., Bressan, A., Chiosi, C., Fagotto, F. and Nasi, E. (1994), 'Theoretical isochrones from models with new radiative opacities', **106**, 275–302.

Bluck, A. F. L., Mendel, J. T., Ellison, S. L. et al. (2016), 'The impact of galactic properties and environment on the quenching of central and satellite galaxies: a comparison between SDSS, Illustris and L-Galaxies', *MNRAS* **462**, 2559–2586.

Bouché, N., Dekel, A., Genzel, R. et al. (2010), 'The Impact of Cold Gas Accretion Above a Mass Floor on Galaxy Scaling Relations', *Astrophysical Journal* **718**, 1001–1018.

Brinchmann, J., Charlot, S., White, S. D. M. et al. (2004), 'The physical properties of star-forming galaxies in the low-redshift Universe', *MNRAS* **351**, 1151–1179.

Bruzual, G. and Charlot, S. (2003), 'Stellar population synthesis at the resolution of 2003', MNRAS **344**, 1000–1028.

Bundy, K., Bershady, M. A., Law, D. R. et al. (2015), 'Overview of the SDSS-IV MaNGA Survey: Mapping nearby Galaxies at Apache Point Observatory', *Astrophysical Journal* **798**, 7.

Bundy, K., Ellis, R. S. and Conselice, C. J. (2005), 'The Mass Assembly Histories of Galaxies of Various Morphologies in the GOODS Fields', *Astrophysical Journal* **625**, 621–632.

Cappellari, M. and Copin, Y. (2003), 'Adaptive spatial binning of integral-field spectroscopic data using Voronoi tessellations', MNRAS **342**, 345–354.

Cardelli, J. A., Clayton, G. C. and Mathis, J. S. (1989), 'The Relationship between Infrared, Optical, and Ultraviolet Extinction', ApJ **345**, 245.

Chabrier, G. (2003), 'Galactic Stellar and Substellar Initial Mass Function', *Publications of the Astronomical Society of the Pacific* **115**, 763–795.

Coenda, V., Martínez, H. J. and Muriel, H. (2018), 'Green valley galaxies as a transition population in different environments', *MNRAS* **473**, 5617–5629.

Connolly, A. J., Szalay, A. S., Bershady, M. A., Kinney, A. L. and Calzetti, D. (1995), 'Spectral Classification of Galaxies: an Orthogonal Approach', AJ **110**, 1071.

Conroy, C. (2013), 'Modeling the Panchromatic Spectral Energy Distributions of Galaxies', ARA&A **51**, 393–455.

Conroy, C., Gunn, J. E. and White, M. (2009), 'The Propagation of Uncertainties in Stellar Population Synthesis Modeling. I. The Relevance of Uncertain Aspects of Stellar Evolution and the Initial Mass Function to the Derived Physical Properties of Galaxies', ApJ **699**, 486–506.

Conroy, C. and Spergel, D. N. (2011), 'On the Formation of Multiple Stellar Populations in Globular Clusters', ApJ **726**.

Conselice, C. J. (2003), 'VizieR Online Data Catalog: Classification of nearby galaxies (Conselice+, 2003)', *VizieR Online Data Catalog* .

Conselice, C. J., Bershady, M. A. and Jangren, A. (2000), 'The Asymmetry of Galaxies: Physical Morphology for Nearby and High- Redshift Galaxies', ApJ **529**, 886–910.

Cox, T. J., Jonsson, P., Primack, J. R. and Somerville, R. S. (2006), 'Feedback in simulations of disc-galaxy major mergers', MNRAS **373**, 1013–1038.

Croom, S. M., Lawrence, J. S., Bland-Hawthorn, J. et al. (2012), 'The Sydney-AAO Multi-object Integral field spectrograph', MNRAS **421**, 872–893.

Croton, D. J., Springel, V., White, S. D. M. et al. (2006), 'The many lives of active galactic nuclei: cooling flows, black holes and the luminosities and colours of galaxies', MNRAS **365**, 11–28.

Daddi, E., Bournaud, F., Walter, F. et al. (2010), 'Very High Gas Fractions and Extended Gas Reservoirs in z = 1.5 Disk Galaxies', *Astrophysical Journal* **713**, 686–707.

Daddi, E., Dickinson, M., Morrison, G. et al. (2007), 'Multiwavelength Study of Massive Galaxies at z˜2. I. Star Formation and Galaxy Growth', *Astrophysical Journal* **670**, 156–172.

Davé, R., Finlator, K. and Oppenheimer, B. D. (2012), 'An analytic model for the evolution of the stellar, gas and metal content of galaxies', *MNRAS* **421**, 98–107.

Dayal, P., Ferrara, A. and Dunlop, J. S. (2013), 'The physics of the fundamental metallicity relation', *MNRAS* **430**, 2891–2895.

Dekel, A., Zolotov, A., Tweed, D. et al. (2013), 'Toy models for galaxy formation versus simulations', *MNRAS* **435**, 999–1019.

Drory, N., MacDonald, N., Bershady, M. A. et al. (2015), 'The MaNGA Integral Field Unit Fiber Feed System for the Sloan 2.5 m Telescope', *Astrophysical Journal* **149**, 77.

Faber, S. M., Willmer, C. N. A., Wolf, C. et al. (2007), 'Galaxy Luminosity Functions to z 1 from DEEP2 and COMBO-17: Implications for Red Galaxy Formation', *Astrophysical Journal* **665**, 265–294.

Fang, J. J., Faber, S. M., Koo, D. C. and Dekel, A. (2013), 'A Link between Star Formation Quenching and Inner Stellar Mass Density in Sloan Digital Sky Survey Central Galaxies', ApJ **776**.

Feldmann, R. (2015), 'The equilibrium view on dust and metals in galaxies: Galactic outflows drive low dust-to-metal ratios in dwarf galaxies', *MNRAS* **449**, 3274–3292.

Geach, J. E., Hickox, R. C., Diamond-Stanic, A. M. et al. (2014), 'Stellar feedback as the origin of an extended molecular outflow in a starburst galaxy', Nature **516**, 68–70.

Geha, M., Blanton, M. R., Yan, R. and Tinker, J. L. (2012), 'A Stellar Mass Threshold for Quenching of Field Galaxies', ApJ **757**.

Genzel, R., Tacconi, L. J., Gracia-Carpio, J. et al. (2010), 'A study of the gas-star formation relation over cosmic time', *MNRAS* **407**, 2091–2108.

Gomes, J. M., Papaderos, P., Vílchez, J. M. et al. (2016), 'Spectroscopic aperture biases in inside-out evolving early-type galaxies from CALIFA', *Astronomy & Astrophysics* **586**, A22.

Guo, Y., Bell, E. F., Lu, Y. et al. (2017), 'CANDELS Sheds Light on the Environmental Quenching of Low-mass Galaxies', ApJ **841**.

Hernández-Toledo, H. M., Vázquez-Mata, J. A., Martínez-Vázquez, L. A. et al. (2008), 'A Morphological Re-Evaluation of Galaxies in Common from the Catalog of Isolated Galaxies and the Sloan Digital Sky Survey (DR6)', AJ **136**, 2115–2135.

Hunter, J. D. (2007), 'Matplotlib: A 2d graphics environment', *Computing In Science & Engineering* **9**(3), 90–95.

Isserstedt, J. and Schindler, R. (1986), 'Spate Galaxien. Die Sternentstehungsraten.', A&A **167**, 11–24.

Jin, Y., Chen, Y., Shi, Y. et al. (2016), 'SDSS-IV MaNGA: properties of galaxies with kinematically decoupled stellar and gaseous components', MNRAS **463**, 913–926.

Kauffmann, G., Heckman, T. M., White, S. D. M. et al. (2003), 'Stellar masses and star formation histories for 10^5 galaxies from the Sloan Digital Sky Survey', *MNRAS* **341**, 33–53.

Kewley, L. J., Groves, B., Kauffmann, G. and Heckman, T. (2006), 'The host galaxies and classification of active galactic nuclei', MNRAS **372**, 961–976.

Kewley, L. J., Heisler, C. A., Dopita, M. A. and Lumsden, S. (2001), 'Optical Classification of Southern Warm Infrared Galaxies', ApJS **132**, 37–71.

Kroupa, P. (2001), 'On the variation of the initial mass function', MNRAS **322**, 231–246.

Le Borgne, J. F., Bruzual, G., Pelló, R. et al. (2003), 'STELIB: A library of stellar spectra at R 2000', A&A **402**, 433–442.

Le Fèvre, O., Saisse, M., Mancini, D. et al. (2003), Commissioning and performances of the VLT-VIMOS instrument, *in* 'Instrument Design and Performance for Optical/Infrared Ground-based Telescopes. Edited by Iye, Masanori; Moorwood, Alan F. M. Proceedings of the SPIE, Volume 4841, pp. 1670-1681 (2003).', Vol. 4841, pp. 1670–1681.

Leonardi, A. J. and Rose, J. A. (1996), 'The Ages of Starbursts in Post-Starburst Galaxies', AJ **111**, 182.

Leonardi, A. J. and Rose, J. A. (2003), 'Analyzing starbursts using magellanic cloud star clusters as simple stellar populations', *The Astronomical Journal* **126**(4), 1811.
URL: *http://stacks.iop.org/1538-3881/126/i=4/a=1811*

Li, C., Wang, E., Lin, L. et al. (2015), 'P-MaNGA: Gradients in Recent Star Formation Histories as Diagnostics for Galaxy Growth and Death', ApJ **804**.

Lilly, S. J., Carollo, C. M., Pipino, A., Renzini, A. and Peng, Y. (2013), 'Gas Regulation of Galaxies: The Evolution of the Cosmic Specific Star Formation Rate, the Metallicity-Mass-Star-formation Rate Relation, and the Stellar Content of Halos', *Astrophysical Journal* **772**, 119.

Liu, C. T. and Kennicutt, Robert C., J. (1995), 'Spectrophotometric Properties of Merging Galaxies', ApJ **450**, 547.

Liu, F. S., Jia, M., Yesuf, H. M. et al. (2018), 'On the Transition of the Galaxy Quenching Mode at 0.5<z<1 in CANDELS', *ArXiv e-prints* .

Liu, F. S., Jiang, D., Guo, Y. et al. (2016), 'The UV-Optical Color Gradients in Star-forming Galaxies at 0.5 < z < 1.5: Origins and Link to Galaxy Assembly', ApJ **822**.

Lotz, J. M., Primack, J. and Madau, P. (2004), 'A New Nonparametric Approach to Galaxy Morphological Classification', AJ **128**, 163–182.

Maeder, A. and Meynet, G. (2000), 'The Evolution of Rotating Stars', ARA&A **38**, 143–190.

Maeder, A. and Meynet, G. (2012), 'Rotating massive stars: From first stars to gamma ray bursts', *Reviews of Modern Physics* **84**, 25–63.

Mihos, J. C. and Hernquist, L. (1994), 'Triggering of starbursts in galaxies by minor mergers', ApJ **425**, L13–L16.

Murtagh, F. and Heck, A., eds (1987), *Multivariate Data Analysis*, Vol. 131 of *Astrophysics and Space Science Library*.

Noeske, K. G., Weiner, B. J., Faber, S. M. et al. (2007), 'Star Formation in AEGIS Field Galaxies since z=1.1: The Dominance of Gradually Declining Star Formation, and the Main Sequence of Star-forming Galaxies', *Astrophysical Journal, Letters* **660**, L43–L46.

Oliphant, T. E. (2015), *Guide to NumPy*, 2nd edn, CreateSpace Independent Publishing Platform, USA.

Pawlik, M. M., Taj Aldeen, L., Wild, V. et al. (2018), 'The origins of post-starburst galaxies at z < 0.05.', MNRAS .

Pawlik, M. M., Wild, V., Walcher, C. J. et al. (2016), 'Shape asymmetry: a morphological indicator for automatic detection of galaxies in the post-coalescence merger stages', *MNRAS* **456**, 3032–3052.

Peng, Y.-j., Lilly, S. J., Kovač, K. et al. (2010), 'Mass and Environment as Drivers of Galaxy Evolution in SDSS and zCOSMOS and the Origin of the Schechter Function', *Astrophysical Journal* **721**, 193–221.

Peng, Y.-j., Lilly, S. J., Renzini, A. and Carollo, M. (2012), 'Mass and Environment as Drivers of Galaxy Evolution. II. The Quenching of Satellite Galaxies as the Origin of Environmental Effects', ApJ **757**.

Rodighiero, G., Daddi, E., Baronchelli, I. et al. (2011), 'The Lesser Role of Starbursts in Star Formation at z = 2', *Astrophysical Journal, Letters* **739**, L40.

Rodighiero, G., Renzini, A., Daddi, E. et al. (2014), 'A multiwavelength consensus on the main sequence of star-forming galaxies at z 2', *MNRAS* **443**, 19–30.

Rose, J. A. (1985), 'Constraints on stellar populations in elliptical galaxies', AJ **90**, 1927–1956.

Salim, S., Rich, R. M., Charlot, S. et al. (2007), 'UV Star Formation Rates in the Local Universe', *Astrophysical Journal Supplement* **173**, 267–292.

Salpeter, E. E. (1955), 'The Luminosity Function and Stellar Evolution.', ApJ **121**, 161.

Sánchez-Blázquez, P., Peletier, R. F., Jiménez-Vicente, J. et al. (2006), 'Medium-resolution Isaac Newton Telescope library of empirical spectra', MNRAS **371**, 703–718.

Sánchez, S. F., Avila-Reese, V., Hernandez-Toledo, H. et al. (2018), 'SDSS IV MaNGA - Properties of AGN Host Galaxies', Rev. Mexicana Astron. Astrofis. **54**, 217–260.

Sánchez, S. F., Pérez, E., Sánchez-Blázquez, P. et al. (2016), 'Pipe3D, a pipeline to analyze Integral Field Spectroscopy Data: II. Analysis sequence and CALIFA dataproducts', Rev. Mexicana Astron. Astrofis. **52**, 171–220.

Schawinski, K., Urry, C. M., Simmons, B. D. et al. (2014), 'The green valley is a red herring: Galaxy Zoo reveals two evolutionary pathways towards quenching of star formation in early- and late-type galaxies', *MNRAS* **440**, 889–907.

Schlegel, D. J., Finkbeiner, D. P. and Davis, M. (1998), 'Maps of Dust Infrared Emission for Use in Estimation of Reddening and Cosmic Microwave Background Radiation Foregrounds', ApJ **500**, 525–553.

Schreiber, C., Pannella, M., Elbaz, D. et al. (2015), 'The Herschel view of the dominant mode of galaxy growth from z = 4 to the present day', *Astronomy and Astrophysics* **575**, A74.

Sérsic, J. L. (1963), 'Influence of the atmospheric and instrumental dispersion on the brightness distribution in a galaxy', *Boletin de la Asociacion Argentina de Astronomia La Plata Argentina* **6**, 41.

Smethurst, R. J., Lintott, C. J., Simmons, B. D. et al. (2015), 'Galaxy Zoo: evidence for diverse star formation histories through the green valley', *MNRAS* **450**, 435–453.

Speagle, J. S., Steinhardt, C. L., Capak, P. L. and Silverman, J. D. (2014), 'A Highly Consistent Framework for the Evolution of the Star-Forming "Main Sequence" from z ˜ 0-6', *Astrophysical Journal, Supplement* **214**, 15.

Strateva, I., Ivezić, Ž., Knapp, G. R. et al. (2001), 'Color Separation of Galaxy Types in the Sloan Digital Sky Survey Imaging Data', *Astronomical Journal* **122**, 1861–1874.

Tacchella, S., Carollo, C. M., Forster Schreiber, N. M. et al. (2017), 'Dust attenuation, bulge formation and inside-out cessation of star-formation in Star-Forming Main Sequence galaxies at z˜2', *ArXiv e-prints* .

Tacchella, S., Dekel, A., Carollo, C. M. et al. (2016), 'The confinement of star-forming galaxies into a main sequence through episodes of gas compaction, depletion and replenishment', *MNRAS* **457**, 2790–2813.

Tacconi, L. J., Genzel, R., Neri, R. et al. (2010), 'High molecular gas fractions in normal massive star-forming galaxies in the young Universe', *Nature* **463**, 781–784.

Takamiya, M. (1999), 'Galaxy Structural Parameters: Star Formation Rate and Evolution with Redshift', *The Astrophysical Journal Supplement Series* **122**, 109–150.

Westera, P., Lejeune, T., Buser, R., Cuisinier, F. and Bruzual, G. (2002), 'A standard stellar library for evolutionary synthesis. III. Metallicity calibration', A&A **381**, 524–538.

Whitaker, K. E., Bezanson, R., van Dokkum, P. G. et al. (2017), 'Predicting Quiescence: The Dependence of Specific Star Formation Rate on Galaxy Size and Central Density at 0.5 < z < 2.5', ApJ **838**.

Whitaker, K. E., Franx, M., Leja, J. et al. (2014), 'Constraining the Low-mass Slope of the Star Formation Sequence at 0.5 < z < 2.5', *Astrophysical Journal* **795**, 104.

Whitaker, K. E., van Dokkum, P. G., Brammer, G. and Franx, M. (2012), 'The Star Formation Mass Sequence Out to z = 2.5', *Astrophysical Journal, Letters* **754**, L29.

Wild, V., Heckman, T. and Charlot, S. (2010), 'Timing the starburst-AGN connection', *MNRAS* **405**, 933–947.

Wild, V., Kauffmann, G., Heckman, T. et al. (2007), 'Bursty stellar populations and obscured active galactic nuclei in galaxy bulges', *MNRAS* **381**, 543–572.

Wild, V., Walcher, C. J., Johansson, P. H. et al. (2009), 'Post-starburst galaxies: more than just an interesting curiosity', MNRAS **395**, 144–159.